Oxidation of a ZrN knee implant coating under in-vitro wear simulation

Citation for the original published paper (version of record):
Rau, J., Eriksson, G., Puente Reyna, A. et al (2025). Oxidation of a ZrN knee implant coating under in-vitro wear simulation. Journal of the Mechanical Behavior of Biomedical Materials, 169. http://dx.doi.org/10.1016/j.jmbbm.2025.107069

Journal of the Mechanical Behavior of Biomedical Materials 169 (2025) 107069

Contents lists available at ScienceDirect

Journal of the Mechanical Behavior of Biomedical Materials

journal homepage: www.elsevier.com/locate/jmbbm

Oxidation of a ZrN knee implant coating under *in-vitro* wear simulation

Julia S. Rau [a,*], Gustav Eriksson [b], Ana Laura Puente Reyna [c], Jens Schwiesau [c,d], Martin Andersson [b], Mattias Thuvander [a]

[a] Department of Physics, Chalmers University of Technology, SE-412 96, Gothenburg, Sweden
[b] Department of Chemistry and Chemical Engineering, Chalmers University of Technology, SE-412 96, Gothenburg, Sweden
[c] Aesculap AG, Research & Development, DE-78532, Tuttlingen, Germany
[d] Ludwig Maximilians University Munich Departement of Orthopaedic Surgery, Physical Medicine & Rehabilitation, Campus Grosshadern, DE-81377, Munich, Germany

ARTICLE INFO

Keywords:
(Tribologically-induced) oxidation
ZrN
Knee implant
In-vitro wear simulation
Transmission electron microscopy

ABSTRACT

Before knee implants are used in clinical applications, *in-vitro* wear simulation is essential for predicting their reliability and longevity. This study investigated the representativeness of *in-vitro* wear simulation concerning oxide formation on a ZrN multilayer-coated knee implant. Four different locations on one *in-vitro* tested sample were analyzed using scanning (transmission) electron microscopy (SEM/TEM). The sample was subjected to 5 million gait cycles according to ISO 14242–1:2002 in newborn calf serum at body temperature, equivalent to ~ 3–5 years *in-vivo*. The formed surface oxides were compared with a previously investigated as-fabricated femoral component and an '*in-vivo*' implant explanted after approximately two years due to early aseptic loosening. The results showed the presence of an oxide on all investigated surfaces with varying thicknesses (15–280 nm). Hence, all oxides were thicker than what would be expected from native oxidation of ZrN. Oxide composition, thickness and microstructure were comparable between *in-vitro* and *in-vivo* samples, except one outlier on the *in-vitro* sample (280 nm thick oxide). However, the distribution of the colored areas was not comparable: the *in-vivo* sample exhibited a non-articulating area completely purplish colored (art. area golden), whereas colored areas on the *in-vitro* sample were distributed inhomogenously. Differences in loading conditions, presence of embedded particles, exposure duration and fluids could explain these variations.

1. Introduction

When exploring new materials, materials combinations or geometries for artificial joint implants, *in-vitro* wear simulators have become indispensable parts of the process (Cheng et al., 2019; International Organization for Standardization., 2023). These pre-clinical tests are conducted according to national regulations and international standards (ASTM, ISO). An essential property of these tests is their capability to generate representative conditions for the tested joint. Wear simulators should provide insights into the tribological performance under various conditions and replicate the same wear evidence on the acting surfaces as seen in the human body. For total knee replacements (TKR), important factors include friction, surface roughness, "[…] loads, velocities, deformation, stress, and lubrication conditions across the scales during gait" (Rothammer et al., 2023). Contacting surfaces subjected to tribological loading often undergo chemical and microstructural changes (Argibay et al., 2017; Fink, 1930; Fischer and Tomizawa, 1985; Haug et al., 2020; Liu et al., 2018; Rau et al., 2021; Rigney and Karthikeyan, 2010). Recently, an oxide layer formed on a ZrN covered knee explant (~2 years, *in-vivo* conditions) was thoroughly studied (Puente Reyna et al., 2023; Rau et al., 2024).

Puente Reyna et al. observed oxidation marks at the articulating area of a ZrN covered knee implant after 5 million cycles under highly demanding activities (HDA) *in-vitro* knee wear simulation (Puente Reyna et al., 2018). These conditions are comparable to approximately 15–30 years within the human body. However, oxygen-rich areas formed on ZrN multilayer-covered *in-vitro* tested implants have not been investigated so far. Understanding the underlying mechanisms will contribute to improve the prediction of the lifetime of TKR. TKRs are "[…] some of the most common surgical procedures worldwide […]" (Evans et al., 2019). However, revision TKRs are expensive (Kassam et al., 2012) and the outcomes are worse than those for primary surgeries (Evans et al., 2019).

The focus of this study is the characterization of the oxide(s) formed

* Corresponding author. Chalmers University of Technology, Department of Physics, Fysikgrand 3, SE-412 96, Gothenburg, Sweden.
E-mail addresses: rau.julia@aol.com, julia.rau@chalmers.se (J.S. Rau), gustav.eriksson@chalmers.se (G. Eriksson), ana_laura.puente_reyna@aesculap.de (A.L. Puente Reyna), jens.schwiesau@aseculap.de (J. Schwiesau), martin.andersson@chalmers.se (M. Andersson), mattias.thuvander@chalmers.se (M. Thuvander).

https://doi.org/10.1016/j.jmbbm.2025.107069
Received 2 February 2025; Received in revised form 20 March 2025; Accepted 19 May 2025
Available online 20 May 2025

on a ZrN-multilayer covered knee implant subjected to *in-vitro* wear simulation. Previous studies on this system primarily examined ion-release and wear behavior of the polyethylene (PE) gliding surface. Surprisingly, the formation of oxides on these samples was either overlooked or not investigated further (Grupp et al., 2013; Puente Reyna et al., 2018) until very recently (Puente Reyna et al., 2023; Rau et al., 2024).

Four different locations were considered: (1) in the articulating area - oxidized and unoxidized and (2) the non-articulating area - oxidized and unoxidized. These will be referred to as the "art. area" or "non-art. area" and "purple" (oxidized) or "golden" (unoxidized). (High resolution) transmission electron microscopy ((HR)TEM) was applied to investigate the surface oxides. The results were then compared with the oxides formed under *in-vivo* conditions on an equivalent multilayer (Rau et al., 2024). This comparison allows to draw conclusions about the representative nature of the lab tests. A common measure to assess the quality of *in-vitro* tests is to compare the PE wear of the gliding surface with *in-vivo* tests. Here, we embark on using a new measure for this comparison: the formation and characteristics of oxides. The research question is: How accurately do *in-vitro* wear simulation tests represent oxide formation within the human body on a ZrN covered knee implant? PE wear for the *in-vitro* sample was already studied in (Grupp et al., 2013; Puente Reyna et al., 2018) and is not part of this paper. Other origins of implant failure, such as implant design or surgical malalignment (Cheng et al., 2019), are not the focus of this research. Understanding the underlying mechanisms of oxide formation on ZrN under both *in-vitro* and *in-vivo* conditions will help manufacturers to improve design guidelines for material and microstructure choice in the long run.

2. Experimental

2.1. Materials

A femoral component from the AS VEGA System® (Aesculap AG, Tuttlingen, Germany), middle size FL4 (left), was investigated. A 3.5–5 μm thick multilayer covers the implant surface (Aesculap® AS Advanced Surface). This physically vapor deposited (PVD) layer consists of a thin adhesive Cr layer, five alternating intermediate layers of CrN and CrCN and a final topmost ZrN layer. More details about this multilayer can be found in previous work (Puente Reyna et al., 2023; Reich et al., 2010). The substrate is a Co-based metal (composition according to ISO 5832–4:2014). In the discussion, the *in-vitro* sample is compared with an *in-vivo* tested sample (size F6R, right) and an as-fabricated implant (size FL4). The manufacturing process for the implants is consistent regardless of the size and there were no changes in the specifications (e.g. geometry and surface finish) for manufacturing the components between the *in-vitro* and the *in-vivo* sample. Due to the extensive and detailed investigation in this work, only one in-vitro tested femoral component was examined. Therefore, the results should be interpreted with this limitation in mind.

2.2. Tribological testing

The *in-vitro* sample was combined with ultra-high weight molecular polyethylene (UHMWPE) gliding surfaces. This test, conducted by Grupp et al. (2013), is briefly summarized here. Counterbody wear was not the focus of this study as it was thoroughly examined in previous studies by Grupp et al. (2013) and Puente Reyna et al. (Puente Reyna et al., 2018). The *in-vitro* sample was tested under physiological loading conditions representative of an average patient (Grupp et al., 2013). A customized, 4-station servo-hydraulic knee wear simulator (Endolab GmbH, Thansau, Germany) was used to perform the wear test, following ISO 14243–1:2002, which simulates the conditions of a 75 kg patient during level walking. The femoral component was subjected to 5 million cycles (compression up to 3 times the body weight) in 20 g/l newborn calf serum (Biochrom AG, Berlin, Germany) at 37 °C, 1 Hz, pH ~ 6. More details are published in (Grupp et al., 2013). This is equivalent to around 3–5 years *in-vivo*. After the wear test, the femoral component was cleaned with soap and deionized water, then air-dried (standard procedure for washing metal components after a wear test). For storage, it was packed in an air-permeable bag in a dark environment (cardbox at room temperature) for 11 years. Prior to this study, no chemical or microstructural analysis was performed on this particular sample. Regions of interest for microstructural and chemical analysis include the art. and non-art. surfaces, as well as the oxidized (purple) and unoxidized (golden) regions. Here, the difference between art. and non-art. area is determined by whether the femoral component is in contact with the PE surface.

2.3. Microstructural and chemical characterization

Samples were cut with two types of low-speed diamond (wire) saws (Buehler IsoMet, Lake Bluff, USA and Well diamond wire saw SA, Switzerland) to fit them into the SEM chamber. Afterwards, all parts were cleaned for 15 min in ethanol and 15 min in acetone. SEM characterization and TEM-foil extraction were performed at a sufficient distance from the cutting edges and at the same locations (black boxes in Fig. 1). For this, the dual beam FIB/SEM (focused ion beam; FEI Versa3D LoVac DualBeam, ThermoFisher Scientific, Waltham, Massachusetts, USA) was used. The first step involved milling of a circle around the region of interest to release any remaining surface stresses (Rau et al., 2024). The foil preparation followed the protocol by (Mayer et al., 2007). Two protective Pt layers (electron-beam, 11 nA, 2 kV and ion-beam 1 nA, 30 kV) were applied within the FIB to minimize ion beam damage. Two TEM-foils were cut at each location, resulting in a total of eight foils. Growth defects from the PVD process on the sample surface were characterized by cutting (FIB milling) cross-section in the middle of the defects to estimate their depth. Energy dispersive X-ray spectroscopy (EDS) measurements of the surfaces were performed with the Tescan GAIA 3 (Tescan, Czech Republic) at 20 kV.

The TEM (FEI Titan 80–300, Thermo Fisher) was operated at 300 kV in STEM and (HR)TEM modes to analyze the TEM-foils. The multilayer thickness was measured within the TEM micrographs. EDS measurements were conducted to obtain chemical information about the surface oxide (tilt angle of 15°, spotsize 1). The TEM Imaging & Analysis (TIA) software was used to quantify the results (foil thickness 100 nm and averaged density 6 g/cm^3). Two maps of the non-art. areas were created using an image size of 25 x 10–18 pixels and a dwell time of 1500–2500 ms.

3. Results

3.1. Optical impressions

The *in-vitro* tested femoral component is depicted in Fig. 1. The ZrN top-most layer has a golden color. Due to its high reflectivity, reflections of the surroundings (e.g. the imaging light, black arrows) are visible. Fig. 1 a + b show two different viewing angles on the same sample. The art. area (1 + 2) and non-art. area (3 + 4) are marked with two black squares. Within these areas, green arrows represent blueish/purplish/reddish and golden regions which are locations where in total four TEM-foils were extracted. Fig. 1c shows a close-up of the colored area on the non-art. area, displaying rainbow-like colors (4). Overall, the entire sample exhibits colored areas distributed inhomogeneously over the whole surface.

3.2. Scanning electron microscopy

SEM(-EDS) provided a general overview of the surface appearance and chemistry with a broader perspective compared to the later used TEM. SEM-EDS maps of the four different surfaces reveal Cr-rich regions of varying sizes on all areas (Fig. 2). Fig. 2e summarizes the chemical

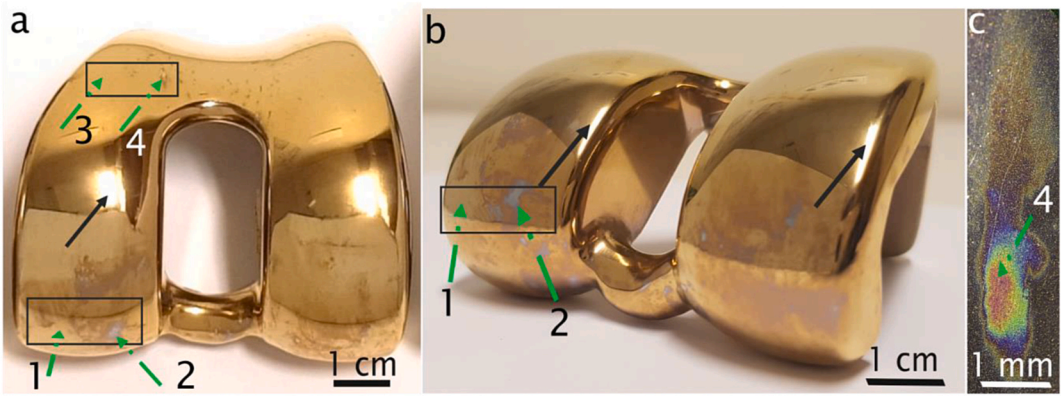

Fig. 1. Photographs of (a) the *in-vitro* sample and (b) a different viewing-angle and close-up of the marked area in (a). Some visible features are due to the reflections during imaging caused by the polished surface. As an example, black arrows mark the reflection of the imaging light. Green arrows represent the locations where the TEM-foils were prepared from. (c) Close-up of region 4 marked in (a) where the TEM-foil was taken from the yellowish/reddish area. The two distinguished areas are the art. area (1 + 2) and non-art. area (3 + 4). Within these areas, one colored (purplish/yellowish/reddish) and one golden region was chosen. (For interpretation of the references to color in this figure legend, the reader is referred to the Web version of this article.)

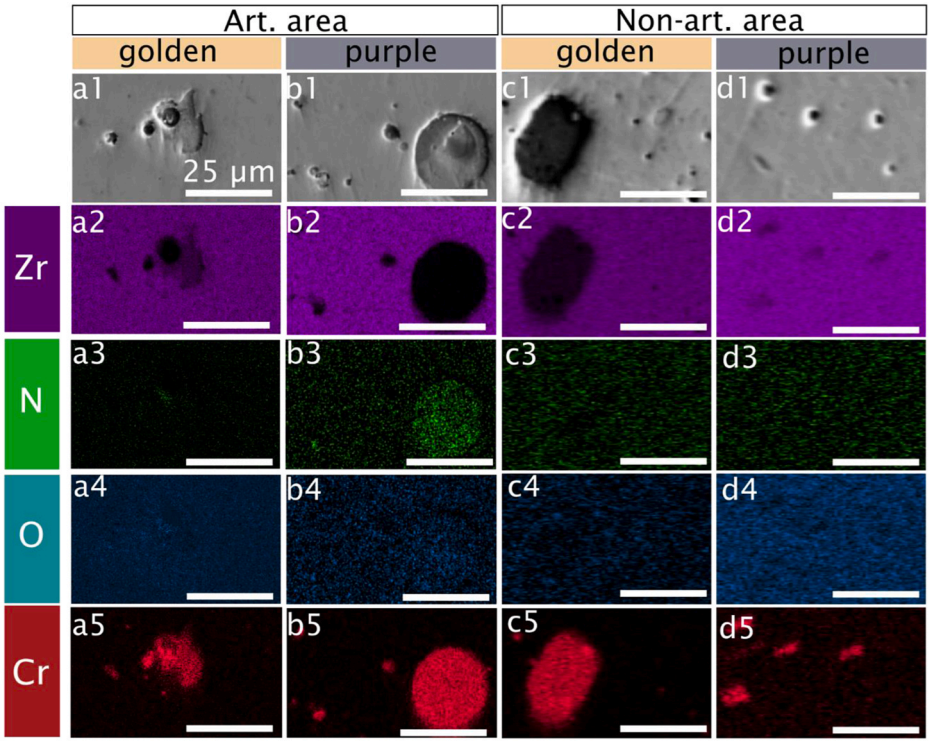

e

at %	Art. area, golden	Art. area, purple	Non-art. area, golden	Non-art. area, purple
Zr	48.6 ± 1.5	35.5 ± 1.1	50.4 ± 2.7	33.0 ± 0.7
N	34.6 ± 3.5	27.2 ± 0.5	34.5 ± 1.7	7.4 ± 0.5
O	16.0 ± 4.9	36.2 ± 1.5	14.0 ± 1.5	58.5 ± 0.3
Cr	0.7 ± 0.1	0.8 ± 0.1	0.8 ± 0.1	0.8 ± 0.1
Co	0.1 ± 0.1	0.3 ± 0.1	0.3 ± 0.1	0.2 ± 0.0

Fig. 2. SEM-EDS data of the surface showing Zr (purple), N (green), O (blue) and Cr (red). The scale bar represents 25 µm. (e) Average chemical composition of the ZrN surface based on 3–5 measurements. (For interpretation of the references to color in this figure legend, the reader is referred to the Web version of this article.)

composition from 3 to 5 point-measurements of the ZrN surface (excl. the Cr-rich regions). Carbon contamination of the surface was deliberately excluded from the results. All locations, except for the Cr-rich regions, contained less than 1 atomic percent (at%) of Cr and Co. The purple areas exhibited higher oxygen concentrations compared to the golden areas. The purple region on the non-art. area had the highest oxygen concentration, reaching up to ~60 at%.

The top-down SEM images in Fig. 3 reveal that the Cr-rich regions

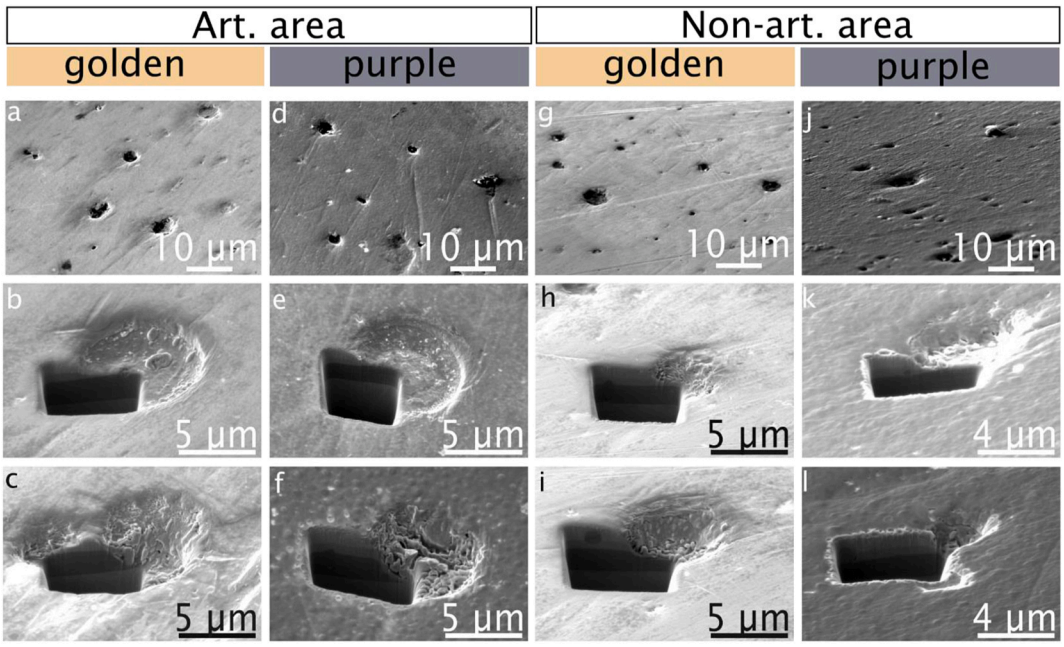

Fig. 3. SEM images of the surfaces highlighting the growth defects. The sample surface was tilted by 52° for all samples except "non-art. area purple", (j–l) which was tilted by 42°. Due to the varying sample curvature, the images in (a,d,g,j) look differently tilted. (b,c,e,f,h,i,k,l) show a cross-section of one side of the crater left behind by a removed growth particle. (For interpretation of the references to color in this figure legend, the reader is referred to the Web version of this article.)

identified in Fig. 2 are actually craters. Growth defects from the PVD multilayer were removed, resulting in craters that extend into the CrN/CrCN layer. The depth of these craters is thus ~2 µm.

3.3. (Scanning) transmission electron microscopy

Since the multilayer is very thin, the high-resolution technique TEM, is applied to provide an overview of the entire multilayer and individual

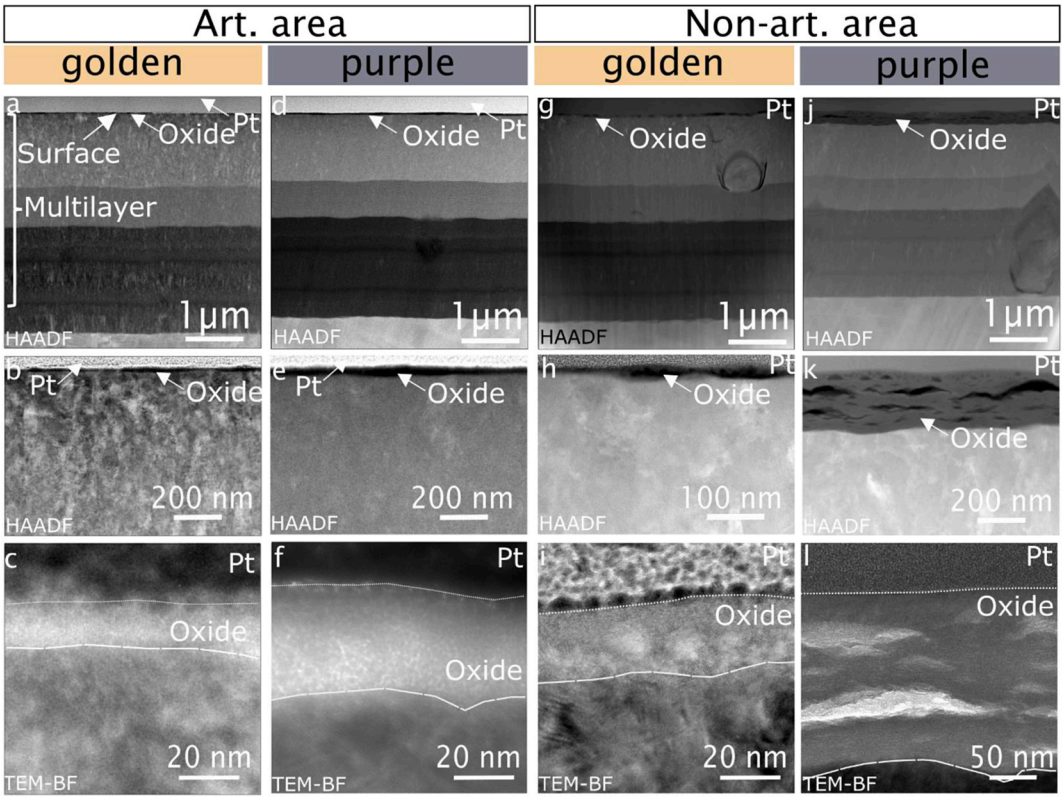

Fig. 4. (S)TEM-images (a–c) on the art. area golden, (d–f) purple, (g–i) non-art. area golden and (j–l) purple. The surfaces were covered by protective platinum applied during the FIB/SEM sample preparation. (a,d,g,j) STEM images in HAADF mode - overview of the entire multilayer, (b,e,h,k) close-ups in HAADF mode of the oxide layer, (c,f,i,l) close-ups of the oxide layers - BF images in transmission mode. (For interpretation of the references to color in this figure legend, the reader is referred to the Web version of this article.)

features within the surface region (Fig. 4, (S)TEM-images in high angle annular dark field (HAADF) or bright field (BF) mode). All surfaces are covered with a very thin layer with a different contrast than the topmost ZrN-layer, indicating a lighter composition. Each surface was coated with a protective Pt-layer (GIS-Pt) applied during the sample preparation inside the FIB/SEM. The total multilayer thicknesses, including oxides, are: 3.9 μm (golden, art. area), 3.6 μm (purple, art. area), 3.8 μm (golden, non-art. area) and 3.4 μm (purple, non-art. area). The surface oxide layers in the golden areas are thinner than those in the purple areas. The oxide layer thicknesses are: ~15–25 nm (golden, art. area), ~25–40 nm (golden, non-art. area), ~30–40 nm (purple, art. area) and up to 280 nm (purple, non-art. area). The multilayer's non-art. area contains inhomogenities that appear like 'particles' within the layer (Fig. 4g,j) which are the growth defects characterized in Figs. 2 and 3. The layer in the non-art. area, purple exhibits wave-like features with a darker contrast in HAADF, indicating a lighter phase (Fig. 4k).

To learn more about the nature of the oxide (e.g. microstructure), high resolution BF-TEM images of the non-art. area purple and golden are shown in Fig. 5. Fig. 5a,b,g represent the overview images, while Fig. 5c–f, h-j display the fast Fourier transforms (FFTs) taken from the marked regions in the overview images. FFTs enable the identification of amorphous vs. (nano-)crystalline regions within a sample. Green squares indicate areas with a diffraction pattern, blue squares represent areas with ring-like patterns and red and purple squares denote areas with fewer diffraction spots compared to the green ones.

Selected area diffraction (SAD) was performed to further investigate the nature of the thickest oxide (Fig. 6). Within the oxide, one exemplary region was chosen (Fig. 6b). The selection of defined spots within the diffraction pattern in the FFTs (Fig. 6c) allows for the identification of locations within the sample that caused those spots. Two areas within the diffraction patterns (Spot 1 and 2) were analyzed to determine whether the oxide is (nano-)crystalline (Spot 1) or amorphous (Spot 2). For both selected spots, bright areas appeared within the oxide and the underlying ZrN (Fig. 6e + g).

Fig. 7 summarizes the STEM-EDS-maps of the surface layers in the non-art. areas for the regions marked in Fig. 7a + e. This analysis provides an impression of the oxide appearance and confirms that darker regions in the HAADF images (Fig. 4b–e,h,k) are oxygen-rich. Fig. 7a–d represent the golden area and Fig. 7e–h represent the purple region. The oxygen-containing region in the golden region is confined to two semicircular regions (Fig. 7d). The upper edges of these semicircles were defined as surface; however, it is difficult to mark the exact interface. In contrast, the layer on the purple region (Fig. 7e–h) is continuous and exhibits a homogenous O concentration.

4. Discussion

4.1. Art. vs. non-art. area

The optical impressions of the femoral component show purplish-colored areas on both the art. and non-art. areas (Fig. 1). The color of ZrN is associated with its oxygen and nitrogen content (Cheng and Zheng, 2006) and various colors are observed for many ZrN coatings (Brown et al., 1993; Niyomsoan et al., 2002; Vaz et al., 2004). For thin oxides, interference colors, which depend on the oxide thickness, are visible (Fig. 1c).

Additionally, removed growth defects from the PVD process were found on all investigated areas (Figs. 2 and 3). Similar regions were identified on two other femoral components covered with the same multilayer: one was an as-fabricated implant, and the other one was an explant (*in-vivo* sample, taken out after ~ 2 years) (Rau et al., 2024). The influence of these defects on the tribological, corrosive and oxidative behavior was already discussed in (Rau et al., 2024).

The overall appearance of the multilayer (excluding the oxides) did not vary significantly between the art. and non-art. area (Fig. 4). The lowest multilayer thicknesses were measured for the purple regions. Specifically, the multilayer thickness was the lowest in the purple sample in the non-art. area with the thickest oxide. Bormann et al.

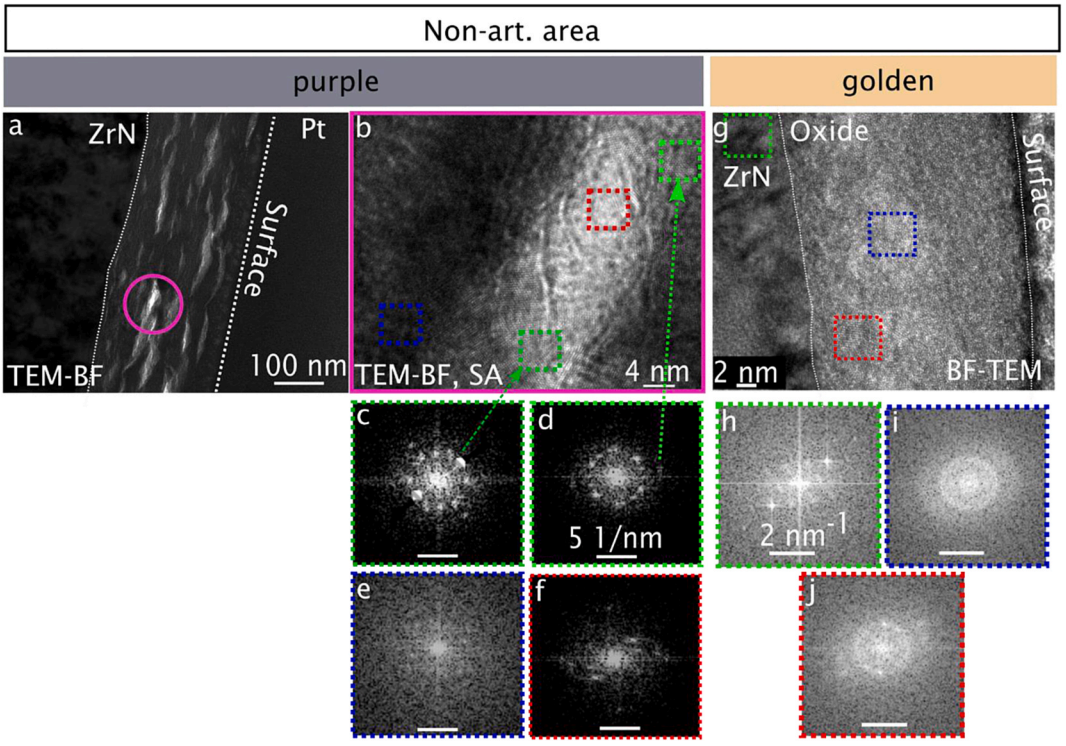

Fig. 5. (High resolution) BF-TEM images of the non-art. area. The surface and oxide/nitride interface are marked by dashed lines. (a–f) Purple areas and (g–j) golden areas. (c-f, h-j) FFTs from the regions marked in (b) and (g). (For interpretation of the references to color in this figure legend, the reader is referred to the Web version of this article.)

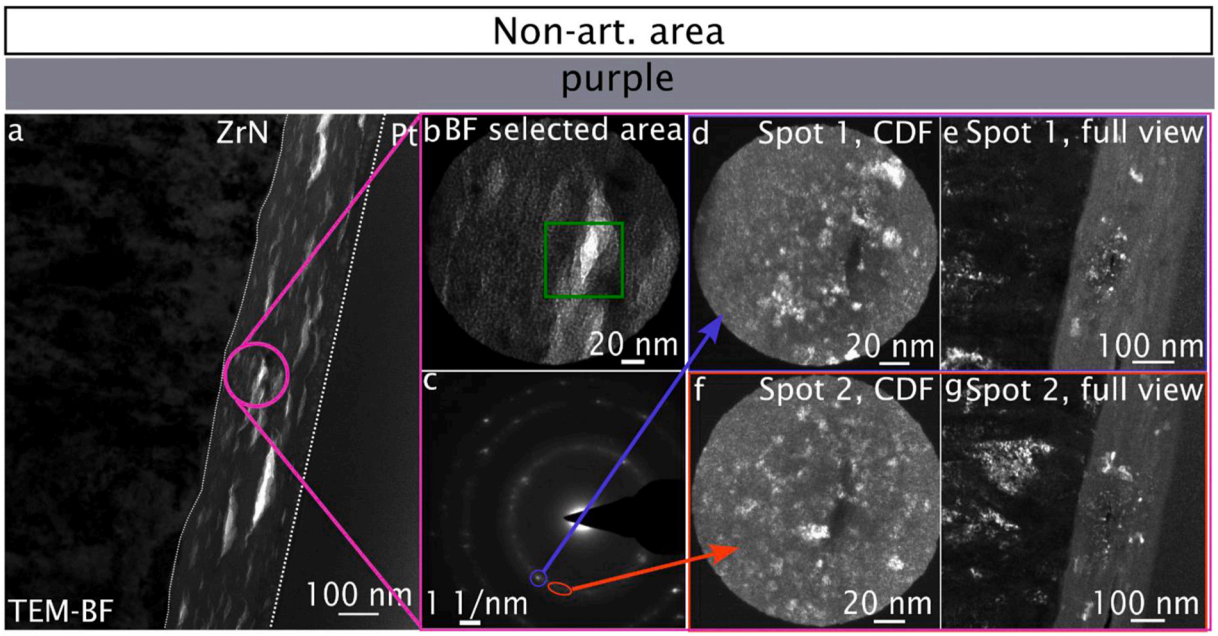

Fig. 6. SAD of the non-art. area (purple). (a) BF-TEM overview. The surface and oxide/nitride interfaces are marked by dashed lines. (b) Selected area within the oxide, the green square marks the area analyzed in Fig. 5a. (c) Diffraction pattern of the selected area in (b). (d) Central dark field (CDF) image of the blue diffraction spot in (c). (e) Full view of the CDF image. (f + g) equivalent to (d + e) for the red region without a clear diffraction spot in (c). (For interpretation of the references to color in this figure legend, the reader is referred to the Web version of this article.)

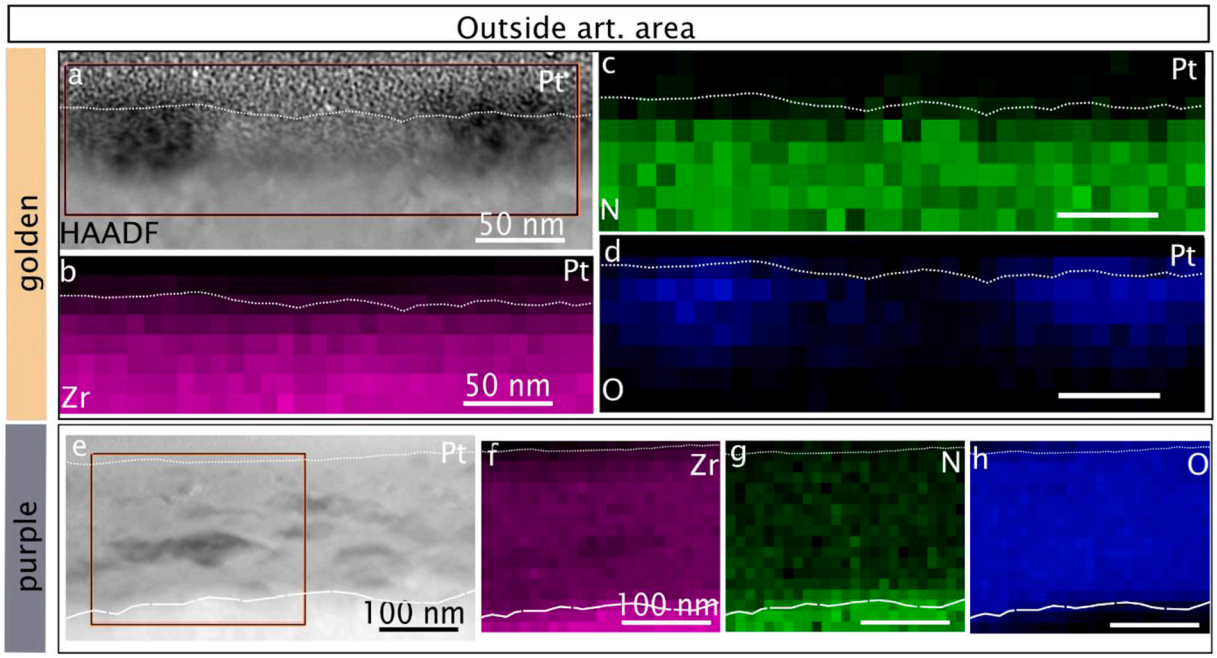

Fig. 7. STEM-EDS maps of the surface layer in the non-art. area, golden and purple. (a,e) STEM-HAADF overviews of the surface layer. (b-d, f-h) EDS maps of the area marked in (a+e) for Zr (purple), N (green) and O (blue). The scale bar for (a–c) represents 50 nm and 100 nm for (e–h). (For interpretation of the references to color in this figure legend, the reader is referred to the Web version of this article.)

studied the reduction in coating thickness for ZrN-covered implants (5 samples) between articulating and non-articulating areas under *in-vivo* conditions (up to 3.6 years) and found an average multilayer thickness reduction of less than 0.5 μm for the articulating area (Bormann et al., 2023). For the locations analyzed here, the multilayer thickness was within the companies' specified range of ~3.5–5 μm. Bormann et al. assumed a homogeneous multilayer thickness over the entire implant surface (Bormann et al., 2023). However, it is unclear whether the multilayer is uniformly thick across the entire surface, so a correlation between a thinner multilayer and thicker oxide formation cannot be established.

4.2. Oxide appearance: golden vs. purple

Golden and purple regions were observed in both the art. and non-art. areas. From the optical and visual impressions, one might assume

that the purple areas are oxidized, while the golden areas are pure ZrN. Interestingly, all four analyzed surfaces exhibited a surface layer associated with oxide formation, with thicknesses greater than expected for native oxidation (Fig. 4). The oxides in the purple areas were thicker than those in the golden regions. The STEM-EDS maps confirm that the layer is oxygen rich (Fig. 7). The oxide thicknesses will be discussed in detail in chapter 4.4.2.

The interface between oxide and the ZrN is sharp, as previously observed for a ZrN covered *in-vivo* sample (Rau et al., 2024). Additionally, the underlying ZrN layer did not undergo any chemical changes, indicating a protective nature of the oxide (Rau et al., 2024). Indeed, Atar et al. reported that oxide formation on ZrN has beneficial effects, such as increased wear resistance and fricition coefficient decrease (Atar et al., 2005). However, the stability of these oxides remains uncertain. As noted in (Rau et al., 2024), the oxides spalled off from the surface when the additional circle-milling step for the TEM-foil sample preparation, mentioned in the experimental section, was not performed. This suggests that these oxides are rather brittle.

4.3. Comparison with an as-fabricated implant

In our previous paper, we investigated an as-fabricated implant covered with the same multilayer as examined here, and observed a very thin, only a few nm thick oxygen containing layer, using atom probe tomography (APT) (Rau et al., 2024). A native oxide layer on ZrN coatings has often been reported in the literature (Milošev et al., 1996, 1997; Prieto et al., 1994; Roman et al., 2011). These layers, formed at room temperature, are very thin (~1.5 – 3.7 nm) (Muneshwar and Cadien, 2018; Prieto et al., 1994) and exhibit self-limiting surface oxidation for exposures >120 min, with a final thickness of 3.7 nm (Muneshwar and Cadien, 2018). Although the *in-vitro* sample had been stored in air for 11 years prior to our investigation, no significant effect from the native oxidation during this time is expected due to this self-limiting effect. All oxygen-containing layers on the *in-vitro* samples were thicker (15–280 nm) than what would be expected for native oxidation. Hence, native oxidation is negligible here and is expected to be homogenous over the entire multilayer and thus cannot explain the differences between the articulating, non-articulating and differently colored areas.

4.4. Comparison with an in-vivo sample

The oxides formed here are compared with a recently investigated *in-vivo* sample (Puente Reyna et al., 2023; Rau et al., 2024) that was explanted due to aseptic loosening after around two years. On the *in-vivo* sample, the art. and non-art. area could clearly be distinguished by their colors. Puente Reyna et al. described a polishing effect responsible for the successive removal of the oxide and multilayer (in some locations, the CrCN/CrN layer was exposed as the ZrN was completely removed) (Puente Reyna et al., 2023). For the *in-vitro* sample, no such polishing effect was visible. In this chapter, the two samples will be compared and in Chapter 4.5, the representativeness of the *in-vitro* test will be discussed.

4.4.1. Oxide color and distribution

From the initial optical impression, the same colors (golden and purplish) appeared on both the *in-vitro* and *in-vivo* sample. However, the distribution of the colors differed. The *in-vitro* sample had colored dots spread across the entire surface, whereas the *in-vivo* sample showed a clear separation between the art. (golden) and non-art. (purple/greyish) areas. TEM and APT revealed oxide formation in both locations (Rau et al., 2024).

4.4.2. Oxide thickness

Oxides were formed at all investigated locations (*in-vivo* and *in-vitro*) with thicknesses greater than expected for native oxidation (summarized in Table 1). This is not surprising, as under tribological loading in a corrosive environment, metals and also nitrides exhibit tribologically-induced oxide formation and changes in surface chemistry (Drnovšek et al., 2016; Liu et al., 2018; Luo, 2010; Rau et al., 2021, 2022; Tkadletz et al., 2014). Sometimes, thickness changes can be orders of magnitude larger than under static conditions due to the normal and shear forces acting on the contact (Rau et al., 2021; Sullivan et al., 1980). For example, oxides 10–50 times thicker were observed on the *in-vivo* sample compared to the as-fabricated implant. With a thickness of 280 nm in the non-art. area, purple (*in-vitro*), this factor is even higher. The *in-vitro* thickness in the art. area golden was the same as in the *in-vivo* art. area golden. It seems that patchier surface oxides, despite having comparable thickness to the colored areas, were not sufficient to generate a color change to purple, possibly because the entire surface was not completely covered in these regions. Using color as reference for the extent of oxidation is overly simplistic, as interference colors are influenced by very small changes in the oxide thickness.

The observed thick oxide on the *in-vitro* sample (non-art. area, purple) represents an outlier. The interference color indicates that this oxide had a varying thickness at this location (Fig. 1c). It remains unclear what caused this large deviation in oxide thickness. Locally, the conditions seemed to be very favorable for forming a thick oxide layer. The multilayer itself did not appear different from other locations, suggesting that a defective multilayer was not the cause. Hence, local conditions might have been different in this area.

4.4.3. Oxide chemistry and microstructure

Table 2 summarizes the SEM-EDS results from Fig. 2e and ref. (Rau et al., 2024). Quantifying light elements with EDS, such as O and N, is challenging and often underestimates their concentrations (Goldstein et al., 2003). In addition, overlapping peaks (e.g. O and Cr) may influence the results. The presence of Cr in all SEM-EDS measurements indicates that some of the underlying CrN/CrCN layers were also measured. Hence, absolute values should be interpreted with caution and are primarily used for comparison.

When comparing the O concentrations for the *in-vivo* and *in-vitro* samples “golden”, they range from 10 to 16 at%. The purple areas exhibited higher concentrations: 44 at% O *in-vivo* and 36 at% *in-vitro* art. area vs. 59 at% non-art. area. The thickest oxide layer formed in the non-art. area and exhibits wave-like structures with varying contrast and brightness. From the STEM-EDS map in Fig. 7h, the oxygen-rich area appears to be relatively homogenous. HR-TEM analysis with FFTs of selected regions within the oxide revealed that the oxides on the non-art. area seem to contain nano-crystalline/amorphous areas (ring-like diffraction patterns and diffraction spots in the FFTs, Fig. 5). However, a more detailed analysis with SAD of the oxide in the non-art. area (Fig. 6) indicated a predominantly nanocrystalline structure. The diffraction pattern (Fig. 6c) from the circular region in Fig. 6a shows a ring-like structure with some brighter spots on those rings. ZrO_2 can have monoclinic, cubic or tetragonal crystal structures, with the tetragonal form usually present between 1440 and 2640 K and cubic form up to the melting point (~2950 K) (J Howard et al., 1988). An attempt to fully index the pattern in Fig. 6c was unsuccessful, as the tetragonal and cubic patterns were too similar. However, the monoclinic structure could be excluded. This indicates the complex influence of local conditions on the

Table 1
Overview of the oxide thickness on the *in-vitro* and *in-vivo* (Rau et al., 2024) femoral components.

Sample	Location	Oxide thickness [nm]
In-vitro	Art. area, golden	15–25
	Art. area, purple	25–40
	Non-art. area, golden	30–40
	Non-art. area, purple	up to 280
In-vivo (Rau et al., 2024)	Art. area, golden	up to 25
	Non-art. area, purple	30–40

Table 2
Overview of the chemical composition of the oxides determined with SEM-EDS in comparison with an as-fabricated implant and an *in-vivo* sample from ref. (Rau et al., 2024).

Method	Unit	Sample	Area	Color	Zr	N	O	Cr
SEM-EDS	at %	As-fabricated implant (Rau et al., 2024)		golden	41	54	4	0.7
		In-vivo (Rau et al., 2024)	Non-art. area	purple	46	10	44	0.4
			Art. area	golden	44	45	10	0.8
		In-vitro	Art. area	golden	49	35	16	0.7
				purple	36	27	36	0.8
			Non-art. area	golden	50	35	14	0.8
				purple	33	7	59	0.8

formed oxide, potentially resulting in a structure that is not thermodynamically stable at room temperature. The insufficient oxygen concentration to form stable ZrO_2 further suggest a possibly metastable structure of the oxide. Fig. 6d–g represent two different spots (blue and red) within the diffraction pattern from Fig. 6c: a brighter diffraction spot and a more ring-like section. For both spots, CDF images were taken within the oxide and the adjacent ZrN (Fig. 6d–g). Bright areas appeared in both the oxide and nitride, indicating that all these regions had a crystalline nature. In conclusion, the purple oxide in the non-art. area appears to be nanocrystalline, leading to this halo-like diffraction pattern.

4.5. Representativeness of the in-vitro test

Often, PE wear patterns are used as measure to compare *in-vivo* and *in-vitro* tests (Harman et al., 2009; Orozco Villaseñor and Wimmer, 2016). Here, the focus is different: How representative are *in-vitro* tests when simulating oxide formation within the human body for a ZrN multilayer-covered knee implant? The *in-vitro* and *in-vivo* samples were compared in the previous chapter. It was found that the differences were in the distribution of colored areas and in the oxide thicknesses. The similarities were that oxides formed on all surfaces were thicker than those formed through native oxidation and all oxides had a lower oxygen concentration than expected for ZrO_2. Here, possible reasons for the observed differences will be discussed.

4.5.1. Representative nature of the selected samples

Before speculating on the possible reasons for the differences between *in-vitro* and *in-vivo* tests, the representativeness of the samples will be discussed. This study compared only three samples: one *in-vivo* sample and one as-fabricated implant that were previously characterized (Puente Reyna et al., 2023; Rau et al., 2024) and the *in-vitro* sample investigated here. Analyzing just one sample for each condition does not provide definitive answers but offers insights for future research.

Choosing the right test conditions for *in-vitro* experiments is heavily researched and debated field, which is not the focus of this work. Some recent findings are briefly summarized as follows:

Stress fields under tribological loading are complex and not yet completely understood (Dollmann et al., 2024). Evidence suggests that actual load components in the human body are much higher than those currently applied in *in-vitro* tests. For instance, Kutzner et al., Bergmann et al. and Mündermann et al. observed much larger differences in peak contacting forces between individuals and different activities (Bergmann et al., 2014; Kutzner et al., 2010; Mündermann et al., 2008). Rothammer et al. found up to a 27 % difference in peak pressures during one gait cycle among three different patients with varying weights, heights, and ages (Rothammer et al., 2023). Studies have shown for PE-wear that "wear phenomena observed after retrieval of TKR do not match the ones from components tested in joint simulators following the ISO 14243-3 […] gait cycle (Harman et al., 2009; Orozco Villaseñor and Wimmer, 2016), suggesting that testing standards might not adequately mimic the actual *in vivo* conditions (Lundberg et al., 2012)" (Rothammer et al., 2023). For example, variations in daily activities originating from different regional or cultural demands create diverse situations. The *in-vitro* tests simulated a patient weight of 75 kg, lighter than the ~100 kg of the *in-vivo* sample's owner. Additionally, the positioning of the femoral component within the patient, which could influence loading conditions, is unknown. Environmental conditions and lubricants also vary among patients, leading to different corrosive conditions (Igual Munoz et al., 2015). As a result, making representative choices of patients and *in-vitro* test conditions remains a challenge.

4.5.2. Representative nature of the in-vitro wear simulation with respect to oxide formation

The primary purpose of the *in-vitro* wear tests was to measure the wear of the PE component, based on the number of steps a person takes per year. These tests were not designed to represent oxidation. This study investigates how well these conditions can simulate the oxide formation.

The *in-vitro* test generated oxides on all surfaces with greater thickness than expected for native oxidation, comparable to the *in-vivo* sample (Rau et al., 2024). However, the distribution of the oxides was less homogenous in the *in-vitro* environment, with more unevenly distributed purple regions.

Several factors may explain these differences. Mechanical loading conditions (e.g. 75 kg vs. 100 kg, see Chapter 4.5.1), the presence of bone cement particles in the PE, exposure time to fluids and the fluid composition are relevant.

The *in-vivo* sample was implanted for ~2 years while the *in-vitro* sample experienced tribological loading equivalent to 3–5 years *in-vivo*. This is represented by 10 weeks of exposure to the testing fluid. Oxidation time is crucial, both when exposed to fluids and under tribological loading (Rau et al., 2021, 2022). This may explain why the oxide in the non-art. area of the *in-vitro* sample was thinner than in the *in-vivo* sample due to different exposure times.

Additionally, the *in-vitro* sample was in constant movement for nearly six days, with no rest period, unlike the *in-vivo* sample, which had resting times (e.g. during sleeping at night, sitting, etc.). After each component analysis interval for the *in-vitro* sample, the test medium was replaced, removing potential wear particles and altering the tribological system.

Moreover, the *in-vitro* test-setup contained another discrepancy: the test chamber was not entirely filled with test medium, exposing parts of the knee to air during flexion, unlike the *in-vivo* sample, which was always in contact with synovial fluid. The lubricating medium also differed (calf serum vs. body fluid). Munoz et al. pointed out "[…] a certain inadequacy of calf serum to reproduce the electrochemical and corrosion behavior of synovial fluids" (Igual Munoz et al., 2015). Bovine calf serum yielded different open circuit potentials and reaction mechanisms in contact with CoCrMo, which could explain differences in the non-art. area, previously associated with "pure" static oxidation and influenced by the surrounding medium (Rau et al., 2024).

In addition, it remains unclear how the presence and distribution of embedded particles within the PE gliding surfaces has influenced the appearance of the *in-vivo* sample (Puente Reyna et al., 2023; Rau et al., 2024). A more uniform distribution of embedded particles might result in more uniform abrasion of the art. surface. The *in-vitro* sample was tested without third-body particles (bone cement particles), meaning the test medium was "clean'. Hence, the specimen only articulated against pure, "soft' PE, which did not polish the femur surface. In contrast, the *in-vivo* PE sample contained bone cement particles that polished the femur's art. area.

In summary, the *in-vitro* test produced oxides with comparable thickness, microstructure, and chemical composition (with the

exception of an outlier with a very thick oxide in the non-art. area). However, the distribution of the oxide was not representative (small regions vs. large areas on the *in-vivo* samples), likely due to differences in loading conditions, exposure durations, lubricating media and the presence of bone cement particles.

5. Conclusions

A ZrN-multilayer coated knee implant was subjected to *in-vitro* wear simulation, designed to mimic human body conditions (e.g. temperature, load, environment). The representativeness of this test was evaluated by analyzing the oxide formation on the outermost ZrN layer and comparing it with an *in-vivo* sample that had been implanted in a patient for approximately two years. The oxides were analyzed optically and with scanning (transmission) electron microscopy, leading to the following observations.

- The entire *in-vitro* implant surface showed purplish areas, which were inhomogeneously distributed on the golden ZrN coating.
- Among the four investigated regions (golden and purple within the articulating area, golden and purple within the non-articulating area), all surfaces had an outermost oxide layer formed that was thicker than native oxides. Purple areas had thicker oxides than golden ones.
- The measured oxygen content of all oxides was below the value of ZrO_2 (~67 at%). The microstructure of the investigated TEM foils contained nanocrystalline areas.
- In comparison with an *in-vivo* implant, the *in-vitro* sample exhibited comparable oxide thicknesses, microstructure, and chemical composition, except for an outlier with a very thick oxide in the non-art. area. However, the overall distribution of the purple area on the ZrN coating was different: the *in-vivo* sample's non-articulating area was completely purple, and its articulating area was golden, whereas the *in-vitro* sample exhibited small purple areas inhomogeneously distributed over the whole sample. The reason for this remains unclear, but it could be speculated that different loading conditions, exposure durations, presence of embedded particles and lubrication media were the main influencing factors.

In the future, this comparison will requiremore statistics and thus more samples for both conditions, rather than relying on just one specimen. It should be emphasized that the *in-vitro* wear test performed with this specimen is intended to evaluate the release of bearing material to estimate mechanical longevity and possible biological reactions, rather than changes in the surface conditions of the bearing materials. Nevertheless, this study highlights that the *in-vitro* wear test can simulate several aspects of the oxide formation on a microscopic scale (structure, composition). For macroscopic changes, further rigorous evaluations are crucial to accurately represent a broad range of *in-vivo* conditions. Moreover, considering all processes occurring within the contact, including oxidation, is essential for a holistic simulation.

CRediT authorship contribution statement

Julia S. Rau: Writing – review & editing, Writing – original draft, Methodology, Investigation, Funding acquisition, Formal analysis, Data curation, Conceptualization. **Gustav Eriksson:** Writing – review & editing, Investigation. **Ana Laura Puente Reyna:** Writing – review & editing, Resources. **Jens Schwiesau:** Writing – review & editing, Resources. **Martin Andersson:** Writing – review & editing, Supervision, Resources. **Mattias Thuvander:** Writing – review & editing, Supervision, Resources.

Data availability

The data that support the findings in this study are available under the https://doi.org/10.5281/zenodo.14724125 (Rau et al., 2025) and from the corresponding author upon request.

Declaration of competing interest

The authors declare the following financial interests/personal relationships which may be considered as potential competing interests: Ana Laura Puente Reyna and Jens Schwiesau are employees of Aesculap AG Tuttlingen, a manufacturer of orthopaedic implants.

Acknowledgments

This work was performed in part at Chalmers Material Analysis Laboratory, CMAL. The Aesculap AG is acknowledged for providing the analyzed material. We thank David Mayweg for the support with the TEM-SAD measurements. Support from the Walter Benjamin fellowship, project Nr. 514540103 and 550653890, provided by the German Research Foundation (DFG) is gratefully acknowledged by JR. MA and GE acknowledge the Wallenberg Foundation and the Swedish Research Council (VR) for their support.

References

Argibay, N., Chandross, M., Cheng, S., Michael, J.R., 2017. Linking microstructural evolution and macro-scale friction behavior in metals. J. Mater. Sci. 52, 2780–2799. https://doi.org/10.1007/s10853-016-0569-1.

Atar, E., Sabri Kayali, E., Cimenoglu, H., 2005. Wear behavior of As-Deposited and oxidized ternary (Zr,Hf)N coatings. Metall. Mater. Trans. 36, 2793–2800. https://doi.org/10.1007/s11661-005-0275-0.

Bergmann, G., Bender, A., Graichen, F., Dymke, J., Rohlmann, A., Trepczynski, A., Heller, M.O., Kutzner, I., 2014. Standardized loads acting in knee implants. PLoS One 9, 1–12. https://doi.org/10.1371/journal.pone.0086035.

Bormann, T., Kraenzler, S., Jaeger, S., Kluess, D., Mittelmeier, W., Renkawitz, T., Kretzer, J.P., 2023. Stability of ceramic coatings on retrieved knee prostheses. J. Mech. Behav. Biomed. Mater. 144, 1–7. https://doi.org/10.1016/j.jmbbm.2023.105997.

Brown, R., Alias, M.N., Fontana, R., 1993. Effect of composition and thickness on corrosion behavior of TiN and ZrN thin films. Surf. Coat. Technol. 62, 467–473. https://doi.org/10.1016/0257-8972(93)90285-V.

Cheng, C.K., Wang, X.H., Luan, Y.C., Zhang, N.Z., Liu, B.L., Ma, X.Y., Nie, M.D., 2019. Challenges of pre-clinical testing in orthopedic implant development. Med. Eng. Phys. 72, 49–54. https://doi.org/10.1016/j.medengphy.2019.08.006.

Cheng, Y., Zheng, Y.F., 2006. A study of ZrN/Zr coatings deposited on NiTi alloy by PIIID technique. IEEE Trans. Plasma Sci. 34, 1105–1108. https://doi.org/10.1109/TPS.2006.877502.

Dollmann, A., Kübel, C., Tavakkoli, V., Eder, S.J., Feuerbacher, M., Liening, T., Kauffmann, A., Rau, J., Greiner, C., 2024. Deformation twins as a probe for tribologically induced stress states. Commun Mater 5, 1–10. https://doi.org/10.1038/s43246-023-00442-8.

Drnovšek, A., Panjan, P., Panjan, M., Čekada, M., 2016. The influence of growth defects in sputter-deposited TiAlN hard coatings on their tribological behavior. Surf. Coat. Technol. 288, 171–178. https://doi.org/10.1016/j.surfcoat.2016.01.021.

Evans, J.T., Walker, R.W., Evans, J.P., Blom, A.W., Sayers, A., Whitehouse, M.R., 2019. How long does a knee replacement last? A systematic review and meta-analysis of case series and national registry reports with more than 15 years of follow-up 655–663. https://doi.org/10.1016/S0140-6736(18)32531-5. www.thelancet.com393.

Fink, M., 1930. Wear oxidation - a new component of wear. Trans. Amer. Soc. for Steel Treating 18.

Fischer, T.E., Tomizawa, H., 1985. Interaction of tribochemistry and microfracture in the friction and wear of silicon nitride. Wear 105, 29–45. https://doi.org/10.1016/0043-1648(85)90004-3.

Goldstein, J.I., Newbury, D.E., Echlin, P., Joy, D.C., Lyman, C.E., Lifshin, E., Sawyer, L., Michael, J.R., 2003. Scanning Electron Microscopy and X-ray Microanalysis. Springer US, Boston, MA. https://doi.org/10.1007/978-1-4615-0215-9.

Grupp, T.M., Saleh, K.J., Mihalko, W.M., Hintner, M., Fritz, B., Schilling, C., Schwiesau, J., Kaddick, C., 2013. Effect of anterior-posterior and internal-external motion restraint during knee wear simulation on a posterior stabilised knee design. J. Biomech. 46, 491–497. https://doi.org/10.1016/j.jbiomech.2012.10.017.

Harman, M.K., Desjardins, J., Benson, L., Banks, S.A., Laberge, M., Hodge, W.A., 2009. Comparison of polyethylene tibial insert damage from *in vivo* function and *in vitro* wear simulation. J. Orthop. Res. 27, 540–548. https://doi.org/10.1002/jor.20743.

Haug, C., Ruebeling, F., Kashiwar, A., Gumbsch, P., Kübel, C., Greiner, C., 2020. Early deformation mechanisms in the shear affected region underneath a copper sliding contact. Nat. Commun. 11, 1–8. https://doi.org/10.1038/s41467-020-14640-2.

Igual Munoz, A., Schwiesau, J., Jolles, B.M., Mischler, S., 2015. *In vivo* electrochemical corrosion study of a CoCrMo biomedical alloy in human synovial fluids. Acta Biomater. 21, 228–236. https://doi.org/10.1016/j.actbio.2015.03.008.

International Organization for Standardization, 2023. ISO 21536:2023 Non-active surgical implants — Joint replacement implants — Specific requirements for knee-joint replacement implants.

J Howard, B.C., Hill, R.J., Reichert, B.E., 1988. Structures of the ZrO 2 polymorphs at room temperature by high-resolution neutron powder diffraction. Acta Cryst B44, 116–120. https://doi.org/10.1107/S0108768187010279.

Kassam, A., Dieppe, P., Toms, A., 2012. An analysis of time and money spent on investigating painful total knee replacements. Br. J. Med. Pract. 5, 1–4.

Kutzner, I., Heinlein, B., Graichen, F., Bender, A., Rohlmann, A., Halder, A., Beier, A., Bergmann, G., 2010. Loading of the knee joint during activities of daily living measured in vivo in five subjects. J. Biomech. 43, 2164–2173. https://doi.org/10.1016/j.jbiomech.2010.03.046.

Liu, Z., Höche, T., Gumbsch, P., Greiner, C., 2018. Stages in the tribologically-induced oxidation of high-purity copper. Scr. Mater. 153, 114–117. https://doi.org/10.1016/j.scriptamat.2018.05.008.

Lundberg, H.J., Ngai, V., Wimmer, M.A., 2012. Comparison of ISO standard and TKR patient axial force profiles during the stance phase of gait. In: Proceedings of the Institution of Mechanical Engineers, Part H: Journal of Engineering in Medicine, pp. 227–234. https://doi.org/10.1177/0954411911431650.

Luo, Q., 2010. Origin of friction in running-in sliding wear of nitride coatings. Tribol. Lett. 37, 529–539. https://doi.org/10.1007/s11249-009-9548-x.

Mayer, J., Giannuzzi, L.A., Kamino, T., Michael, J., 2007. TEM sample preparation and FIB-induced damage. MRS Bull. 32, 400–407. https://doi.org/10.1557/mrs2007.63.

Milošev, I., Strehblow, H.H., Gaberščček, M., Navinšek, B., 1996. Electrochemical oxidation of ZrN hard (PVD) coatings studied by XPS. Surf. Interface Anal. 24, 448–458. https://doi.org/10.1002/(SICI)1096-9918(199607)24:7<448::AID-SIA137>3.0.CO;2-F.

Milošev, I., Strehbtow, H.-H., Navinšek, B., 1997. Comparison of TiN, ZrN and CrN hard nitride coatings: electrochemical and thermal oxidation. Thin Solid Films 303, 246–254. https://doi.org/10.1016/S0040-6090(97)00069-2.

Mündermann, A., Dyrby, C.O., D'Lima, D.D., Colwell, C.W., Andriacchi, T.P., 2008. In vivo knee loading characteristics during activities of daily living as measured by an instrumented total knee replacement. J. Orthop. Res. 26, 1167–1172. https://doi.org/10.1002/jor.20655.

Muneshwar, T., Cadien, K., 2018. Comparing XPS on bare and capped ZrN films grown by plasma enhanced ALD: effect of ambient oxidation. Appl. Surf. Sci. 435, 367–376. https://doi.org/10.1016/j.apsusc.2017.11.104.

Niyomsoan, S., Grant, W., Olson, D.L., Mishra, B., 2002. Variation of color in titanium and zirconium nitride decorative thin films. Thin Solid Films 415, 187–194. https://doi.org/10.1016/S0040-6090(02)00530-8.

Orozco Villaseñor, D.A., Wimmer, M.A., 2016. Wear scar similarities between retrieved and simulator-tested polyethylene TKR components: an artificial neural network approach. BioMed Res. Int. 1–10. https://doi.org/10.1155/2016/2071945, 2016.

Prieto, P., Galán, L., Sanz, J.M., 1994. Interaction of oxygen with ZrN at room temperature: an XPS study. Surf. Interface Anal. 21, 395–399. https://doi.org/10.1002/sia.740210612.

Puente Reyna, A.L., Fritz, B., Schwiesau, J., Schilling, C., Summer, B., Thomas, P., Grupp, T.M., 2018. Metal ion release barrier function and biotribological evaluation of a zirconium nitride multilayer coated knee implant under highly demanding activities wear simulation. J. Biomech. 79, 88–96. https://doi.org/10.1016/j.jbiomech.2018.07.043.

Puente Reyna, A.L., Lützner, J., Altermann, B., Grupp, T.M., 2023. Analysis of the In vivo oxidation and integrity of a zirconium nitride multilayer coated knee implant and possible effect of oxidation on the implant-cement-bone interface fixation strength. International Case Reports Journal 3, 1–16.

Rau, J., Eriksson, G., Puente Reyna, A.L., Schwiesau, J., Andersson, M., Thuvander, M., 2025. Raw data to manuscript on "Oxidation of a ZrN Knee Implant Coating under In-vitro Wear Simulation". Zenodo. https://doi.org/10.5281/zenodo.14724125 [Data set].

Rau, J.S., Balachandran, S., Schneider, R., Gumbsch, P., Gault, B., Greiner, C., 2021. High diffusivity pathways govern massively enhanced oxidation during tribological sliding. Acta Mater. 221, 1–9. https://doi.org/10.1016/j.actamat.2021.117353.

Rau, J.S., Eriksson, G., Malmberg, P., Reyna, A.L.P., Schwiesau, J., Andersson, M., Thuvander, M., 2024. Oxidation of a zirconium nitride multilayer-covered knee implant after two years in clinical use. Acta Biomater. 190, 593–604. https://doi.org/10.1016/j.actbio.2024.10.034.

Rau, J.S., Schmidt, O., Schneider, R., Debastiani, R., Greiner, C., 2022. Three regimes in the tribo-oxidation of high purity copper at temperatures of up to 150°C. Adv. Eng. Mater. 24, 1–13. https://doi.org/10.1002/adem.202200518.

Reich, J., Hovy, L., Lindenmaier, H.L., Zeller, R., Schwiesau, J., Thomas, P., Grupp, T.M., 2010. Preclinical evaluation of coated knee implants for allergic patients. Orthopä 39, 495–502. https://doi.org/10.1007/s00132-009-1581-9.

Rigney, D.A., Karthikeyan, S., 2010. The evolution of tribomaterial during sliding: a brief introduction. Tribol. Lett. 39, 3–7. https://doi.org/10.1007/s11249-009-9498-3.

Roman, D., Bernardi, J., Amorim, C.L.G.D., De Souza, F.S., Spinelli, A., Giacomelli, C., Figueroa, C.A., Baumvol, I.J.R., Basso, R.L.O., 2011. Effect of deposition temperature on microstructure and corrosion resistance of ZrN thin films deposited by DC reactive magnetron sputtering. Mater. Chem. Phys. 130, 147–153. https://doi.org/10.1016/j.matchemphys.2011.06.013.

Rothammer, B., Wolf, A., Winkler, A., Schulte-Hubbert, F., Bartz, M., Wartzack, S., Miehling, J., Marian, M., 2023. Subject-specific tribo-contact conditions in total knee replacements: a simulation framework across scales. Biomech. Model. Mechanobiol. 22, 1395–1410. https://doi.org/10.1007/s10237-023-01726-1.

Sullivan, J.L., Quinn, T.F.J., Rowson, D.M., 1980. Developments in the oxidational theory of mild wear. Tribol. Int. 13, 153–158. https://doi.org/10.1016/0301-679X(80)90031-6.

Tkadletz, M., Mitterer, C., Sartory, B., Letofsky-Papst, I., Czettl, C., Michotte, C., 2014. The effect of droplets in arc evaporated TiAlTaN hard coatings on the wear behavior. Surf. Coat. Technol. 257, 95–101. https://doi.org/10.1016/j.surfcoat.2014.01.010.

Vaz, F., Carvalho, P., Cunha, L., Rebouta, L., Moura, C., Alves, E., Ramos, A.R., Cavaleiro, A., Goudeau, P., Rivière, J.P., 2004. Property change in ZrNxOy thin films: effect of the oxygen fraction and bias voltage. Thin Solid Films 469–470, 11–17. https://doi.org/10.1016/j.tsf.2004.06.191.